Proceedings of the Fifteenth Electronics New Zealand Conference ENZCon 2008
24-25 November 2008, Auckland, pp 13-18.

# Electrical Capacitance Tomography Using Bayesian Inference

**Colin Fox**[1] **Daniel Watzenig**[2]

[1] Department of Physics, University of Otago, PO Box 56, Dunedin, New Zealand
[2] Institute of Electrical Measurement and Measurement Signal Processing,
Graz University of Technology, Kopernikusgasse 24, A-8010 Graz, Austria

Email: fox@physics.otago.ac.nz & daniel.watzenig@tugraz.at

**Abstract:** Electrical capacitance tomography is a non-invasive imaging technique that uses measured trans-capacitances outside a medium to recover the unknown permittivity in the medium. We use Bayesian inference to solve the problem of recovering the unknown shape of a constant permittivity inclusion in an otherwise uniform background. Calculated statistics give accurate estimates of inclusion area, and other properties, when using measured data.

**Keywords:** Electrical capacitance tomography (ECT), Bayesian inference, Inverse problem, Markov chain Monte Carlo (MCMC), Prior modelling

## 1. INTRODUCTION

Electrical capacitance tomography (ECT) is a technique for recovering the spatially-varying permittivity of an insulating medium from measurement of capacitance outside the boundary of the medium. ECT is primarily used for non-invasive imaging within inaccessible domains in applications where differing materials show up as contrasting permittivities. Electrodes are set in an insulating material at the outside of an insulating pipe. By applying a predefined voltage pattern to electrodes the capacitance between pairs of electrodes can be directly related to measured electric potentials, electric currents, and electric charges.

Measurements consist of all the capacitances between pairs of electrodes, making up the matrix of trans-capacitances. The interior of the pipe contains the material with unknown permittivity distribution that is being imaged. Measured capacitances depend on the unknown permittivity. The imaging problem is to 'invert' this relationship to determine the unknown permittivity.

ECT has been proposed for a variety of target applications such as imaging dilute as well as bulky multi-phase flows in oil refinement, in the food industry, and to observe pharmaceutical and chemical processes [1, 2, 3, 4]. ECT systems can be implemented with low cost, and due to their robustness and small probability of failure are suitable for operation under harsh conditions, such as imaging in combustion chambers [5] or in the presence of strong external electromagnetic fields [6].

We present a solution to a problem in ECT, of recovering the unknown shape of a single inclusion with unknown constant permittivity in an otherwise uniform background material [7]. This problem arose in an application with the goal of quantifying void fraction (water/air) in oil pipe lines. We apply Bayesian inference to formulate the inverse problem as an estimation problem over the posterior distribution for unknown permittivity conditioned on measured data. Key components of the formulation are a prior model requiring a parametrization of the permittivity and a normalizable prior density, the likelihood function that follows from a decomposition of measurements into deterministic and random parts, and numerical simulation of noise-free measurements. We present the posterior distribution of inclusion area as a check on accuracy of the method.

## 2. INSTRUMENTATION FOR ECT

Two measurement principles are used in ECT instrumentation [8]:

- charge or displacement-current based measurements (a.c. voltage, low-impedance measurement)
- potential based measurements (d.c. voltage, high-impedance measurement)

For both methods each electrode is designated as a 'transmitting' or as a 'receiving' electrode with a prescribed voltage being applied to transmitting electrodes. In the charge-based method the receiving electrodes are held at virtual earth with the displacement charge being measured, while in the voltage-based approach the receiving electrodes are floating with the potential being measured.

The measurements used in this paper were made with the charge-based sensor built at Graz University of Technology [9]. Figure 1 shows the measurement configuration. The front-end of the charge-

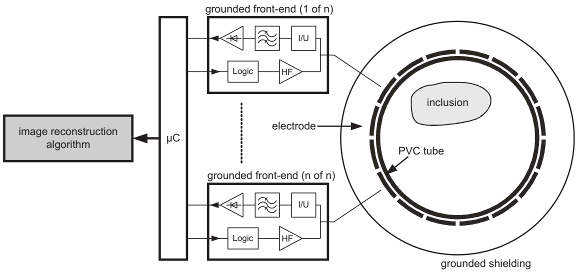


Figure 1: Measurement configuration for ECT. Electrodes are placed around the pipe in the imaging plane. Each electrode features dedicated transmitting and receiving hardware.

based ECT sensor consists of an input resonant circuit, a low-noise current-to-voltage converter, a bandpass filter, a logarithmic demodulator, and a 24 bit analog-to-digital converter controlled by a microprocessor. The sensor has a carrier frequency of 40 MHz and comprises two tuneable filters adjusted by means of variable capacitances for stray capacitance compensation.

### *2.1 Measurement Uncertainty*

The sensor front-end and the subsequent instrumentation introduce noise sources to the measurement process. Applied voltage also has error, but this error is not significant and we don't consider that here (see [10] for an analysis that does). To investigate the robustness and repeatability of data acquisition, the distribution of the measured displacement currents was examined over multiple measurement with a given a fixed permittivity distribution [7]. Figure 2 shows the normalized quantile plot and the histogram for 2000 measurements at one electrode. The measured electrode displacement currents exhibit noise properties that can be well modelled as additive zero mean Gaussian with standard deviation $\sigma \approx 0.07\mu$A. The matrix of sample correlation coefficients for all electrodes is shown in Figure 3. As can be seen, off-diagonal elements are plausibly zero, so the measurement error covariance matrix is modelled as $\Sigma = \sigma^2 I$ where $I$ is the identity matrix. Accordingly, the density for measuring $d$ given permittivity defined by $\theta$ is the multivariate Gaussian,

$$\pi(d|\theta) \propto \exp\left\{-\frac{1}{2}(q_m - d)^T \mathbf{\Sigma}^{-1}(q_m - d)\right\} \quad (1)$$

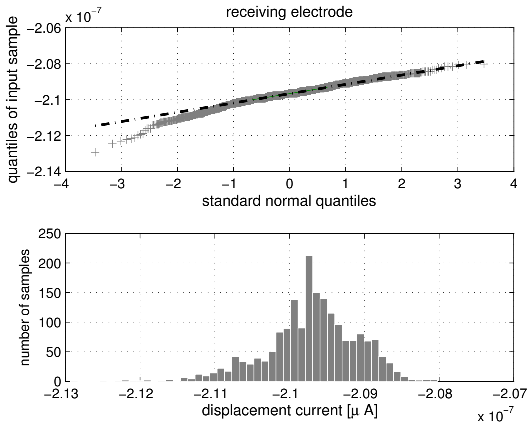


Figure 2: Distribution of 2000 measured displacement currents on one electrode. The distribution can be well modelled as Gaussian distribution according to the normalized quantile plot (top) and the histogram of the displacement currents (bottom).

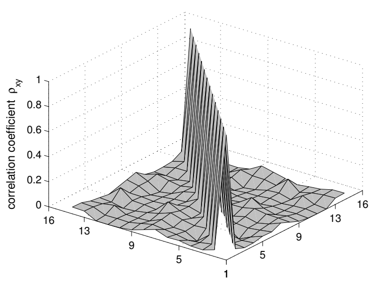


Figure 3: Matrix of correlation coefficients. Off-diagonal elements are almost zero.

where $q_m$ denotes the vector of simulated displacement currents (or charges).

## 3. DATA SIMULATION

We denote the measurement region by $\Omega$, being the region bounded by the electrodes and outer shield. Let $\Gamma_i$, $i = 1, 2, \ldots, N_\mathrm{e}$ denote the boundary of electrode $i$ when there are $N_\mathrm{e}$ electrodes, and let $\Gamma_\mathrm{s}$ be the *inner* boundary of the outer shield. Then the boundary to $\Omega$ is $\partial\Omega = \cup_{i=1}^{N_\mathrm{e}}\Gamma_i \cup \Gamma_\mathrm{s}$. In the absence of internal charges, the electric potential $u$ satisfies the generalized Laplace equation in which the permittivity $\varepsilon$ appears as a coefficient, along with Dirichlet boundary value conditions corresponding to the voltage asserted at electrodes.

For the case when electrode $i$ is held at potential $v_0$ while all others are held at virtual earth, then the potential $u_i$ satisfies the Dirichlet boundary value problem (BVP),

$$\begin{aligned} \nabla \cdot (\varepsilon \nabla u_i) &= 0, & &\text{in } \Omega, \\ u_i|_{\Gamma_i} &= v_0, & & \\ u_i|_{\Gamma_j} &= 0, & & j \neq i, \\ u_i|_{\Gamma_e} &= 0. & & \end{aligned} \tag{2}$$

For brevity we have not written $\varepsilon(r)$ and $u_i(r)$ showing the functional dependence on position $r \in \Omega$, but take that spatial variation to be implicit. The charge at the sensing electrode $j$ can be determined by integration of the electric displacement over the electrode boundary,

$$q_{i,j} = -\oint_{\Gamma_j} \varepsilon \frac{\partial u_i}{\partial n} \mathrm{d}r \tag{3}$$

where $n$ is the inward normal vector.

Our computer solution of the BVP uses a coupled finite element method (FEM) and boundary element method (BEM) scheme [11, 7], with the region being imaged using a BEM formulation coupled to a FEM discretization of the insulating pipe and region outside the electrodes.

## 4. BAYESIAN INFERENCE

In the Bayesian formulation, inference about $\theta$ is based on the posterior density

$$\pi(\theta|d) = \frac{\pi(d|\theta)\pi(\theta)}{\pi(d)}. \tag{4}$$

where $\pi(d|\theta)$ is the likelihood function (for fixed $d$) in equation 1, and $\pi(\theta)$ denotes the prior density expressing the information of $\theta$ prior to the measurement of $d$. The denominator $\pi(d) = \int_\theta \pi(d|\theta)\pi(\theta)d\theta$ is a finite normalizing constant, since our formulation for ECT is fixed, that does not need to be calculated as we can work with the non-normalized posterior distribution.

### *4.1 Representation and Prior Modelling*

Our solution uses a polygonal representation of the boundary, so the permittivity is defined by the parameter $\theta = ((x_1, y_1), (x_2, y_2), \ldots, (x_n, y_n))$ giving the vertexes of an $n$-gon for some fixed $n$ typically in the range 8 to 32. We also include the two permittivity values, but we will omit that consideration here for clarity. A basic prior density over this representation is to sample each vertex $(x_k, y_k)$ uniformly in area from the allowable domain $\Omega$ and restrict to simple polygons, i.e. not self crossing. This prior density has the form

$$\pi(\theta) \propto I(\theta) \tag{5}$$

where $I$ is the indicator function for $\theta$ representing a feasible polygon. That is, the prior density is constant over allowable polygons. The change of variables relation for probability distributions shows that a uniform density in vertex position gives a density over area that scales as $(\text{area})^{-1/2}$. Hence for large polygons, and inclusions, where most polygons are simple, this prior puts greater weight on small areas resulting in estimated areas that will always be smaller than the true area. The constraint that the polygon be simple complicates this picture for small area inclusions, since a greater proportion of small polygons are self crossing. The overall effect is that the area of large inclusions will be underestimated while the area of small inclusions will be overestimated, with the division between 'small' and 'large' depending on the number of vertexes $n$. This effect necessarily occurs in regularized or least-squares fitting of contour-based models, since effectively the constant prior model is used.

Since we are primarily interested in area of inclusions, we explicitly specify a prior in terms of area, given in equation (6) [12]. Denote the circumference of the inclusion by $c(\theta)$ and the area of the polygon by $\Gamma(\theta)$. The prior density is

$$\pi(\theta) \propto \exp\left\{ -\frac{1}{2\sigma_{\text{pr}}^2} \left( \frac{c(\theta)}{2\sqrt{\Gamma(\theta)\pi}} - 1 \right) \right\} I(\theta) \tag{6}$$

in which the variance $\sigma_{\text{pr}}^2$ is chosen to penalize small and large areas.

### *4.2 Posterior Exploration*

The product of equations 1 and 6 gives the non-normalized posterior distribution distribution that we explore to learn about the unknown permittivity. Exploration of the posterior distribution is performed using Markov chain Monte Carlo (MCMC) sampling that generates a Markov chain with equilibrium distribution $\pi(\cdot|d)$ by simulating an appropriate transition kernel [13].

The standard Metropolis-Hastings (MH) algorithm has been extended to deal with transitions in state space with differing dimension [13], allowing insertion and deletion of parameters. Even though we do not use variable-dimension states in the example we prefer this 'reversible jump', or Metropolis-Hastings-Green (MHG), formalism as it greatly simplifies calculation of acceptance probabilities for the subspace moves that we employ.

The reversible jump formalism considers the composite parameter $(\theta, \gamma)$ where $\theta$ is the usual state vector, and $\gamma$ is the vector of random numbers used to compute the proposal $\theta'$. Similarly, $(\theta', \gamma')$ is the composite parameter for the reverse proposal.

Then the MCMC sampling algorithm with MH dynamics can be written as:
*Let the chain be in state $\theta_n = \theta$, then $\theta_{n+1}$ is determined in the following way*:

- *Propose a new candidate state $\theta'$ from $\theta$ with some proposal density $q(\theta, \theta')$*
- *Calculate the MH acceptance ratio*

$$\alpha(\theta, \theta') = min\left(1, \frac{\pi(\theta'|d)q(\gamma')}{\pi(\theta|d)q(\gamma)}\left|\frac{\partial(\theta', \gamma')}{\partial(\theta, \gamma)}\right|\right) \tag{7}$$

- *Set $\theta_{n+1} = \theta'$ with probability $\alpha(\theta, \theta')$ , i.e. accept the proposed state, otherwise set $\theta_{n+1} = \theta$, i.e. reject.*
- *Repeat*

The last factor in equation 7 denotes the Jacobian determinant of the transformation from $(\theta, \gamma)$ to $(\theta', \gamma')$.

We find a combination of $M = 4$ moves gives a suitably efficient MCMC in this example [7]. These are translation, rotation, and scaling of the polygon, and moving the position of one vertex of the polygon. The vertex move ensures irreducibility but, by itself, would lead to a very slow algorithm. The remaining moves are designed to give an efficient algorithm. A new candidate $\theta'$ is proposed from $\theta$ by randomly choosing one of these four moves and using a random step size $\lambda^i$ tuned for each move. The Jacobian term in the MHG algorithm for the moves translation, rotation, and vertex move is 1. For the scaling move the Jacobian term is $\lambda^{-2n+1}$ [7].

## 5. RESULTS

In the following different shaped material inclusions are recovered from simulated and measured data using MCMC sampling. For all experiments inclusions with different shapes and a permittivity of $\varepsilon_r = 3.5$ in an air-filled pipe ($\varepsilon_r = 1.0$) are considered. For the experiments using synthetic data 2,000,000 samples were drawn from the posterior distribution, using a simulated data set corrupted by noise. The data was created using 10,000 boundary elements in the forward map. For the experiment using measured data 1,000,000 samples were drawn from a posterior distribution. Noise standard deviation in both cases was $\sigma = 6.7 \times 10^{-4}$.

A *burn-in period* of 50000 samples was found suitable after testing the algorithm with different initial states and different ratios of moves. During the burn-in-period, which strongly depends on the initial state of the Markov chain, the sampling distribution is not the equilibrium distribution. Once the chain is in equilibrium only every 100th sample is stored. For the results presented, the four proposal moves were chosen with equal probability, giving an acceptance rate of about 2 %.

### *5.1 Experiment 1 – elliptic and fancy-shaped contour (simulated data)*

Figure 4(a) and Figure 4(b) illustrate the resultant posterior variability in inclusion shape for an elliptical inclusion and a more fancy shape, respectively. The figures show scatter plots, constructed by plotting one point randomly from each state, uniformly in boundary length, and gives a graphical display of the probability density that a boundary passes through any element of area. Points in the scatter plot are clustered around the true contour plotted in dashed gray. Due to the decreased sensitivity in the center of the pipe, the margin of deviation of scattered points for the elliptic contour is greater towards the center than in the region close to the electrodes. For the fancy contour

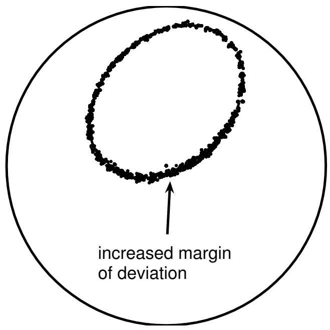


(a)

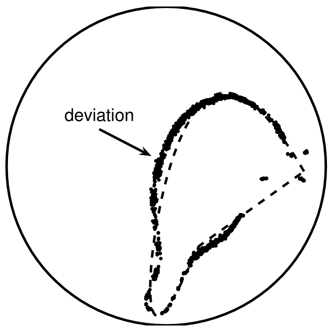


(b)

Figure 4: Scatter plots. (a) Entire domain $\Omega$ with elliptic-shaped inclusion. (b) fancy-shaped contour.

in Figure 4(b) deviations from the true contour in regions of low sensor sensitivity are clearly visible. Furthermore, there are significant outliers in the right part of the estimation result despite this part of the contour being close to the boundary. The reason is that the distinct corner in the true boundary which is not well modelled by our prior, which rejects candidate states with sharp angles between two boundary elements. Note, however, that this mis-modelling in the prior is evident from the scatter plot in the region near the sharp corner, and indicates the significant benefit of posterior error estimates available in a Bayesian analysis.

### *5.2 Experiment 2 – circular contour (measured data)*

Figure 5(a) shows the posterior variability in inclusion shape and position for measured data. Samples from the posterior distribution are consistent with the circular shape of the PVC rod. Due to the lack of a reference measurement system, the true shape is not depicted. However, knowing the geometry of the rod allows validation of the reconstruction results by comparing estimates to the true area and circumference. The centered gray circle-shaped contour represents the initial state of the Markov chain. MAP state and CM state estimates are presented in Figure 5(b). In accordance with the first example (same shape and properties but synthetic data) MAP and CM estimates almost coincide indicating that the posterior distribution has a well-defined single mode. Table 1 summarizes the inference. Mean, standard deviation and the integrated auto-correlation time (IACT) are evaluated for inclusion area $\Gamma$, circumference $c$ and center coordinates $(x, y)$ of the circular inclusion. The integrated auto-correlation time is, roughly, the number of correlated samples with the same variance reducing power as one independent sample. Hence a small IACT indicates a statistically efficient Markov chain.

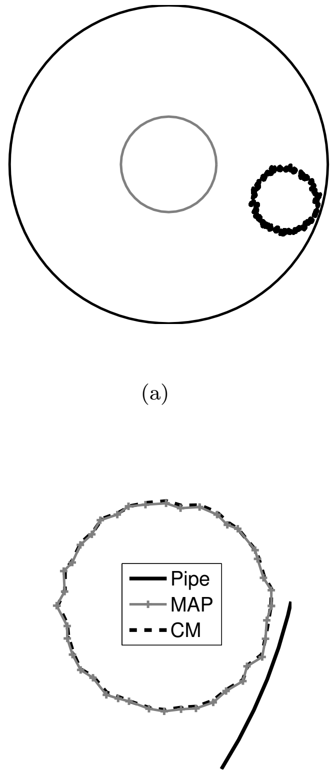


Figure 5: Reconstruction results. (a) Scatter plot. Randomly chosen points of the posterior distribution are plotted. (b) Detail plot of point estimates. MAP estimate (gray) and the CM estimate (dashed black) calculated from the posterior distribution.

## 6. DISCUSSION AND CONCLUSION

The predominant approach to inverse problems in ECT is based on various deterministic iterative (e.g. regularized least squares) or non-iterative (e.g. linear back projection) approximations for image reconstruction.

Inferential solutions to inverse problems provide substantial advantages over deterministic methods, such as the ability to treat arbitrary forward maps and error distributions, and to use a wide range of representations of the unknown system including parameter spaces that are discrete, discontinuous, or even variable dimension.

Markov chain Monte Carlo sampling (MCMC) has revolutionized computational Bayesian inference and is currently the best available technology for a comprehensive analysis of inverse problems, allowing quantitative estimates and exploration of high-dimensional posterior distributions without special mathematical structure. An impediment to the application of Bayesian analyses to practical inverse problems lies in the computational cost of MCMC sampling. In recent years several promising algorithms and advances have been suggested that give substantial speedup for computationally intensive problems including capacitance tomography. There is some hope that eventually the computational cost of sampling will not be substantially greater than that of optimization.

We demonstrated sample-based recovery of a single inclusion with unknown shape and unknown constant permittivity from measured and simulated electrical capacitance data. The accuracy of results speak for themselves.

There is now a range of well-developed tools for stochastic modelling and Bayesian inference for inverse problems. Notwithstanding application-specific modelling difficulties, applying those tools is now a well-defined procedure. The interested

Table 1: Output statistics for circular inclusion estimated from measured data

| Quantities | true values | mean | standard deviation | IACT |
|---|---|---|---|---|
| $x$-coordinate of center [m] | – | $3.71\times10^{-2}$ | $2.32\times10^{-5}$ | $5.89\times10^{2}$ |
| $y$-coordinate of center [m] | – | $-1.14\times10^{-2}$ | $3.02\times10^{-5}$ | $4.65\times10^{2}$ |
| Area $\Gamma$ [m$^2$] | $3.14\times10^{-4}$ | $3.13\times10^{-4}$ | $6.88\times10^{-6}$ | $1.10\times10^{3}$ |
| Circumference c [m] | $6.28\times10^{-2}$ | $6.24\times10^{-2}$ | $1.57\times10^{-4}$ | $1.88\times10^{3}$ |
| Log-likelihood | – | -46.10 | $1.72\times10^{-1}$ | $3.99\times10^{2}$ |

reader can learn more from two local sources: This paper is a (very) abridged version of a tutorial review that the authors recently completed [14]. The modelling and computational methods for Bayesian inference that we apply in this paper have been taught for more than a decade in the graduate course ‘Physics 707 Inverse Problems’ at Auckland University. In 2009 that course will be taught both in Auckland and Otago (under the moniker ELEC 404) with an on-line text available via the latter course.

## 7. REFERENCES


[1] D. S. Holder, *Electrical impedance tomography: methods, history and applications* (Series in Medical Physics and Biomedical Engineering, IOP Publishing Ltd) 2005.

[2] T. York, “Status of electrical tomography in industrial applications,” *Jnl. of Electronic Imaging* 10 pp 608-619, 2001.

[3] H. S. Tapp, A. J. Peyton, E. K. Kemsley and R. H. Wilson, “Chemical engineering applications of electrical process tomography,” *Jnl. of Sensors and Actuators B*, 92, pp 17-24, 2003.

[4] J. C. Gamio, J. Castro, L. Rivera, J. Alamillia, F. Garcia-Nocetti and L. Aguilar, “Visualisation of gas-oil twophase flow in pressurised pipes using electrical capacitance tomography,” *Flow Meas. and Instr.*, 16, pp 129-134 2005.

[5] R. C. Waterfall, “Imaging combustion using electrical capacitance tomography,” *Advanced Sensors and Instr. Systems for Combustion Processes*, pp 12/1-12/4, 2000.

[6] T. Dyakowski, “Application of electrical capacitance tomography for imaging industrial processes,” *Jnl. of Zhejiang University Science*, 12, pp 1374-1378, 2005.

[7] D. Watzenig *Bayesian inference for process tomography from measured electrical capacitance data*, (PhD thesis, Graz University of Technology) 2006.

[8] B. Kortschak, H. Wegleiter and B. Brandstätter, “Formulation of cost functionals for different measurement principles in nonlinear capacitance tomography,” *Meas. Sci. and Techn.*, 18, pp 71-78, 2007.

[9] H. Wegleiter, A. Fuchs, G. Holler and B. Kortschak, “Development of a displacement current based sensor for electrical capacitance tomography applications,” *Flow Measurement and Instrumentation*, 19, pp 241-250, 2008.

[10] C. Fox, G. Nicholls and M. Palm, “Efficient solution of boundary-value problems for image reconstruction via sampling,” Jnl. of Electronic Imaging, 9, pp 251-259, 2000.

[11] B. Kortschak and B. Brandstätter, “A FEM-BEM approach using level-sets in tomography,” *Jnl. for Comp. and Math. in Electrical and Electronic Eng.*, 24, pp 591-605, 2004.

[12] D. Watzenig and C. Fox, “Posterior variability of inclusion shape based on tomographic measurement data,” *Jnl. of Phys.: Conf. Series, 6th Int. Conf. on Inverse Problems in Eng.: Theory and Practice, Paris, France, June 15 - 19*, 2008 (in press).

[13] P. J. Green, “Reversible jump Markov chain Monte Carlo computation and Bayesian model determination,” *Jnl. Biometrika*, 82, 711-732, 1995.

[14] D. Watzenig and C. Fox, “A review of statistical modelling and inference for electrical capacitance tomography,” *Meas. Sci. and Techn.*, 2008 (invited review, submitted).